Computational Fermi level engineering and doping-type conversion of Mg:Ga_2O_3 via three-step synthesis process

Anuj Goyal[1], Andriy Zakutayev[1], Vladan Stevanović[1,2], Stephan Lany[1]

[1]*National Renewable Energy Laboratory, Golden, CO, 80401, United States.*
[2]*Colorado School of Mines, Golden, CO, 80401, United States*

Abstract

Gallium oxide (Ga_2O_3) is being actively explored for electronics that can operate at high power, temperature, and frequency, as well as for deep-ultraviolet optoelectronics and other applications, due to its ultra-wide band gap (UWBG) and low projected fabrication cost of large-size and high-quality crystals. Efficient *n*-type doping of monoclinic beta-phase of Ga_2O_3 has been achieved, but *p*-type doping faces fundamental obstacles due to compensation, deep acceptor levels, and the polaron transport mechanism of free holes. However, aside from the challenges of achieving *p*-type conductivity, plenty of opportunity exists to engineer the position of the Fermi level for improved design of Ga_2O_3 based devices. We use first-principles defect theory and defect equilibrium calculations to simulate a 3-step growth-annealing-quench synthesis protocol for hydrogen assisted Mg doping in β-Ga_2O_3. The simulations take into account the gas phase equilibrium between H_2, O_2 and H_2O, which determines the H chemical potential. We predict Ga_2O_3 doping-type conversion to a net *p*-type regime after growth under reducing conditions in the presence of H_2 followed by O-rich annealing, which is a similar process to the Mg acceptor activation by H removal in GaN. For equilibrium annealing with re-equilibration of compensating O vacancies, there is an optimal temperature that maximizes the Ga_2O_3 net acceptor density for a given Mg doping level; the acceptor density is further increased in the non-equilibrium annealing scenario without re-equilibration. After quenching to operating temperature, the Ga_2O_3 Fermi level drops below mid-gap down to about 1.5 eV above the valence band maximum, creating a significant number of uncompensated neutral Mg_{Ga}^0 acceptors. The resulting free hole concentration in Ga_2O_3 is very low even at elevated operating temperature (~10^8 cm^{-3} at 400C) due to deep energy level of these Mg acceptors, and hole conductivity is further impeded by the polaron hopping mechanism. However, the Fermi level reduction and suppression of free electron density in this doping type converted ($N_A > N_D$) Ga_2O_3 material is important for improved designs of Ga_2O_3 electronics devices. These results illustrate the power of computational predictions not only for new materials but also for their synthesis science.

I. Introduction

The monoclinic beta-phase of gallium oxide (β-Ga_2O_3) is an exciting material for various (opto)electronic and energy-related technologies due to its ultra-wide band gap (UWBG, ~4.9 eV) and the ability to grow large-size high-quality single crystals at low projected cost[1,2]. Considered applications include various power electronic devices[3], radio-frequency transistors[4,5], solar-blind photo-detectors[6–8], gas sensors[9,10], contact layers in photovoltaics[11,12], and other applications[13,14]. In power electronics, dedicated efforts in recent years towards improving crystal growth, *n*-type doping, and device fabrication led to substantial progress in performance of β-Ga_2O_3 based horizontal transistors, vertical Schottky barrier diodes (SBDs), vertical metal oxide semiconductor field effect transistors (MOSFETs), and related devices[15–17]. For example, depletion mode (normally-on) current aperture vertical β-Ga_2O_3 MOSFETs with implantation doping[17] and enhancement-mode (normally-off) Ga_2O_3 vertical transistors with fin-shaped channels[18] have been demonstrated. However, one of the biggest challenges in realizing the true potential of Ga_2O_3 in power electronics, along with its low thermal conductivity, is the absence of *p*-type doping, limiting the design of device structures that can be realized[16].

Ga_2O_3 is intrinsically an *n*-type semiconductor. Using extrinsic donors its *n*-type conductivity is easily tunable over many orders of magnitude[1,19–23], but *p*-type doping faces fundamental obstacles[24–31]. Among various acceptor dopants in Ga_2O_3, Mg is computationally predicted to be the most stable[27] and was also experimentally found to reduce the unintentional *n*-type conductivity and increase the resistivity of the material[26]. Mg doped Ga_2O_3 has been synthesized[32] and studied[33] using an electron paramagnetic resonance (EPR) technique, where Mg acceptor (0/1-) level is experimentally determined to be at E_V+0.7 eV. However, in a photoluminescence study[34], the Mg acceptor level is shown to be deeper at E_V+1.0 eV, which compares better with the theoretical predictions employing hybrid functional calculations[25,28,35,36], where (0/1-) level is estimated to be between E_V+1.0 to 1.5 eV. The differences in theoretical predictions published in literature originate to some extent from different fraction of exact (non-local) exchange employed in these hybrid functional calculations. In more recent computational work, focus has been towards studying diffusion[28], EPR[37] and luminescence properties[38] of Mg doped Ga_2O_3.

The prospects of achieving *p*-type conductivity through acceptor doping in β-Ga_2O_3 remain bleak. However, ample opportunities exist for Fermi level engineering of Ga_2O_3 power electronic devices via acceptor-type dopants[1,16,26]. Even when holes remain localized at the acceptor site or as small polarons, the doping can cause the acceptor concentration (N_A) to exceed the donor concentration (N_D). The result is a doping type conversion with a large drop of the Fermi level E_F where electrons become minority carriers. The resulting acceptor-doped Ga_2O_3 material can be used as buried electron barrier, a.k.a. current blocking layer, for controlling the turn-on voltage and saturation current of vertical metal-oxide-semiconductor field effect transistors (MOSFET) with current aperture. Such acceptor-doped Ga_2O_3 can be also used for increasing the breakdown voltage and decreasing the leakage current of vertical MOSFET and Schottky diodes using edge termination and related structures[1,16,17,26,39]. It is likely that such acceptor doped β-Ga_2O_3 can be achieved using non-equilibrium synthesis process with mobile hydrogen species that was instrumental in achieving *p*-type doping of GaN, which led to the development of the blue light emitting diode.[40–44] More recently, non-equilibrium processing involving hydrogen and oxygen was

employed to reduce the electron density in otherwise degenerately doped $ZnSnN_2$[45,46] and $MgZrN_2$.[47]

Here we computationally predict H-assisted Mg doping of β-Ga_2O_3 under non-equilibrium growth and annealing process, in a broad analogy to the well-known strategies for activating *p*-type conductivity in Mg-doped GaN thin films, using first principles supercell calculations and thermodynamic defect equilibrium simulations. Although traditional *p*-type conductivity resulting from thermal ionization of free holes at room temperature remains beyond reach in Ga_2O_3, we report quantitative computational predictions for synthesis process conditions that lower the Fermi level and enable doping type conversion in Ga_2O_3. The doping-type conversion to a net *p*-type regime is predicted after O-rich annealing of Ga_2O_3 grown under reducing conditions in the presence of H_2. The doping type converted Ga_2O_3 has Fermi level 1.5 eV above the valence band maximum due to uncompensated neutral Mg_{Ga}^0 acceptors, but the resulting free hole concentration is very low (~10^8 cm^{-3} even at 400C) due to deep energy level of these acceptors. These theoretical predictions are expected to guide experimental tuning of growth and annealing conditions to achieve doping type converted Ga_2O_3 for realization of novel device configurations. The results presented in this work illustrate that computations can predict synthesis conditions necessary to synthesize and dope new materials.

II. Approach and methods

As illustrated in Figure 1, our approach consists of a three-step process of (1) thin-film growth under O-poor conditions in the presence of hydrogen, (2) acceptor activation via annealing in an O-rich/H-poor atmosphere, and (3) quenching to a range of operating temperatures. The thermodynamic simulations take into account the $H_2 + ½O_2 \leftrightarrow H_2O$ gas phase equilibrium connecting the O and H chemical potentials. In the first growth step, the presence of H donor impurities can increase the solubility of substitutional Mg_{Ga} acceptors, and it reduces the concentrations of compensating O vacancies (V_O) while the system remains *n*-type. In the second annealing step, meant to purge the mobile H donor species and activate Mg_{Ga} acceptors, we consider two different stages of non-equilibrium. In the more readily realizable scenario, only the equilibration of the Mg solubility is suppressed. In the second scenario, which might be more difficult to realize, also the equilibration of V_O formation is suppressed, thereby allowing for maximal non-equilibrium activation of acceptor dopants and ensuing Fermi level reduction. In the third quenching step, it is assumed that all dopant and defect concentrations remain at the level of the preceding annealing step, and only the Fermi level (E_F) and the corresponding electron and hole densities are equilibrated to the operating temperature of the device.

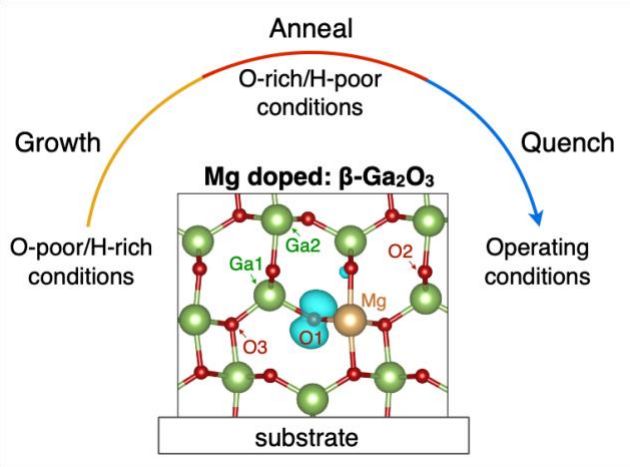

Figure 1. Schematic illustration of thermodynamic conditions in the modeling of growth, annealing, and quenching steps of Mg-doped β-Ga_2O_3. The atomic structure model shows the spin-density iso-surface (blue) associated with the defect-bound hole-polaron created by the neutral Mg_{Ga}^0 acceptor at a neighboring O site.

A. Supercell calculations

The stable phase β-Ga_2O_3, depicted in Fig. 1, has a monoclinic crystal structure (space group C2/m) with two non-equivalent crystallographic Ga sites (Ga1 tetrahedral, and Ga2 octahedrally coordinated) and three O sites (O1 bonded to one Ga1 and two Ga2, O2 bonded to two Ga1 and one Ga2, and O3 bonded to one Ga1 and three Ga2). We included the native defects (V_{Ga}, V_O), extrinsic dopants (Mg_{Ga}, Mg_i, H_i) and defect pairs and complexes (Mg_{Ga}+V_O, 2Mg_{Ga}+V_O, Mg_{Ga}+H_i) expected to form due to charge compensation. The formation energies $\Delta H_D = \Delta H_{ref} + q\Delta E_F + \Sigma_i n_i \Delta\mu_i$ of defects and complexes in a charge state q were calculated using the approach of Ref[48], combining density functional theory (DFT) supercell energies with *GW* band gap corrections (E_g = 4.96 eV) and fitted elemental reference energies[49] (FERE). The binding energies of complexes, shown in Table 1, are determined by subtracting the ΔH_D of the constituents. The Fermi level is taken relative to the valence band maximum (VBM), $\Delta E_F = E_F - E_{VBM}$, and the chemical potentials of the elements i added (n_i = –1) or removed (n_i = +1) by defect formation are taken relative to the FERE, $\Delta\mu_i = \mu_i - \mu_i^{FERE}$. The numerical values for the defect formation energy ΔH_{ref} at the reference point ($\Delta E_F = \Delta\mu_i = 0$) are given in Table 2 in the section "computational details" below. During the thermodynamic simulations (see below), ΔH_D is determined on the fly for the actual Fermi level position and chemical potentials.

The formation energy of Mg_{Ga} is about 0.5 eV lower on the Ga2 site than on Ga1 (see Table 2), implying a strong site preference for the sixfold coordinated site. Figure 1 shows the spin-density of the Mg_{Ga} defect in the neutral charge state, illustrating the localized nature of the hole trapped in the deep acceptor level. Due to the delocalization error of DFT such polaronic states are not captured with standard DFT functionals[50], and we used a hybrid functional to calculate the (0/1–) charge transition level, located 1.0 and 1.1 eV above the VBM for Mg_{Ga2} and Mg_{Ga1}, respectively. For Mg_{Ga2}, the acceptor-hole is localized on the neighboring O1 site (see Fig. 1), in agreement with an experimental EPR study[51]. A standard DFT functional with the above-

mentioned band gap corrections is used otherwise. Oxygen vacancies in Ga_2O_3 act as deep donors, with a negative-U type (2+/0) charge transition in the upper part of the band gap. This transition carries over into the defect pairs with a (1+/1−) transition for a pair with one Mg acceptor and a (0/2−) level for the complex with 2 acceptors (*cf*. Table 2). The hydrogen interstitial H_i acts as shallow donor and assumes the 1+ charge state throughout the range of Fermi energies in the bandgap (the effective-mass donor level close to the CBM is not relevant for this study). In principle, H can also substitute for oxygen (H_O),[22] but we find that the formation energy of H_O is 0.5 eV higher than that of H_i even under the extreme limit of O poor conditions ($\Delta\mu_{Ga} = 0$, $\Delta\mu_O = -3.75$ eV), and we will therefore not further consider H_O in this study. The results of the supercell calculations reported here are consistent with prior literature results.[22,24] Table 1 shows that the binding of the H interstitial to Mg acceptors is weaker than the binding of O vacancies, suggesting that H interstitials are more easily separated from the acceptors during annealing and activation than the O vacancies.

Table 1: Calculated binding energies ΔE_b of the most relevant dopant-defect complexes.

Defect complex	ΔE_b (eV)
$(Mg_{Ga2} + V_{O1})^+$	−0.74
$(Mg_{Ga2} + V_{O2})^+$	−0.58
$(Mg_{Ga2} + V_{O3})^+$	−0.62
$(Mg_{Ga2} + H_i)^0$	−0.44
$(2Mg_{Ga2} + V_{O1})^0$	−1.03
$(2Mg_{Ga2} + V_{O3})^0$	−1.06

B. Thermodynamic modeling

The calculated defect formation energies along with the binding energies of defect pairs are used as an input into our thermodynamic modeling[52,53], which yields quantitative defect concentrations, doping limits, and the position of the Fermi level E_F as function of dopant (Mg) concentration, the partial pressures of oxygen (pO_2), hydrogen (pH_2) or water vapor (pH_2O), and the temperature (T). The Fermi level is obtained as a self-consistent solution that observes the charge balance between defect charges and free carriers, while the defect concentrations are obtained from the defect formation energies for the same E_F. Using the FERE values of Ref.[49], we obtain the formation enthalpy of Ga_2O_3 as $\Delta H_f(Ga_2O_3) = 2\Delta\mu_{Ga} + 3\Delta\mu_O = -11.26$ eV, which defines the relationship between Ga and O chemical potentials under the phase-coexistence of Ga_2O_3. Similarly, using the tabulated[54] formation enthalpy of water vapor, we have $\Delta H_f(H_2O) = 2\Delta\mu_H + \Delta\mu_O - \Delta\mu_{H2O} = -2.48$ eV, where the $\Delta\mu$ values for the gas phases are calculated as function of T and partial pressure via the ideal gas equations with the tabulated standard enthalpies and entropies for 298K and 1 atm (note, $\Delta\mu_O = ½\,\Delta\mu_{O2}$ and $\Delta\mu_H = ½\,\Delta\mu_{H2}$).

In this general thermodynamic modeling approach, non-equilibrium effects are incorporated by suppressing the equilibration of specific processes (dopant exsolution, vacancy formation), while equilibrating the remaining ones. Thus, our work is in principle agnostic to the specific synthesis and doping approach and applies to all methods that allow for some control over these degrees of freedom, including both ion implantation and particularly selective area epitaxy[55] in thin-film

growth for formation of contacts and other functional layers in the device. Similar thermodynamic simulations have been successfully employed in the past in other oxides to quantitatively predict carrier concentrations as a function of synthesis and measurement conditions, for example in case of the non-equilibrium origin of conductivity in Ga doped ZnO[56].

III. Growth step

In Ga_2O_3, as in other wide gap oxides, it is generally observed that annealing in oxygen rich environment reduces the free electron density, while annealing in hydrogen rich environment increases it[1]. This behavior reflects general doping principles[57], where O-rich conditions reduce the formation energy of electron compensating defects like cation vacancies and O interstitials. H-rich environments promote the formation of donor-like H interstitials[58] but at the same time, exposure to H_2 gas also creates O-poor reducing conditions due to the gas phase equilibrium with water vapor, a well-established process that is frequently used in solid state chemistry[59]. These reducing conditions generally favor *n*-type conductivity. According to the doping principles, the increased Fermi energy in *n*-type material reduces the formation energy of acceptor-type dopants, thereby enhancing their solubility. Finally, the mobile nature of H interstitials allows to exploit non-equilibrium processing, such as the removal of hydrogen by annealing while the equilibration of other processes remains suppressed, like the exsolution of acceptor dopants or the formation of compensating intrinsic defects[44]. These concepts are exploited in our initial growth step illustrated in Fig. 2.

Figure 2a shows the equilibrium solubility of Mg as function of temperature and pO_2. Under equilibrium conditions, Hydrogen addition is equivalent to maintaining a certain partial pressure pH_2O of water vapor, and the hydrogen chemical potential ($\Delta\mu_H$) is determined by the gas phase equilibrium as described above. In Fig. 2a, we used $pH_2O = 10^{-5}$ atm as an estimated upper bound for a typical physical vapor deposition (PVD) process such as molecular beam epitaxy (MBE), but the solubility of Mg is barely affected at this low level of hydrogen addition. The Mg equilibrium solubility increases with increasing temperature and decreasing pO_2 (both of which reduce $\Delta\mu_O$) as expected from the doping principles and remains in the sub-percent range except under extreme reducing conditions.

Figure 2b shows defect equilibria as function of the Mg doping level and the hydrogen chemical potential $\Delta\mu_H$, which is controlled by pH_2O (*cf*. left and right vertical axes in Fig 2b), assuming growth conditions at T_g = 600 °C and $pO_2 = 10^{-9}$ atm, as representative for low *T* and moderate pO_2 conditions for PVD (MBE) growth of Ga_2O_3[60]. The solid line in Fig. 2b marks the equilibrium thermodynamic solubility limit of Mg in Ga_2O_3 determined by the competing phase $MgGa_2O_4$. Within the range of data shown in Fig 2b, the Mg chemical potential does not exceed the bounds determined by $Mg(OH)_2$, MgH_2, MgO, and metallic Mg. We observe that significant increases of the Mg solubility occur at $pH_2O > 10^{-5}$ atm, reaching about Mg/(Mg+Ga) = 0.1% at pH_2O = 1 atm, which is feasible in atmospheric pressure chemical vapor deposition processes (APCVD) of β-Ga_2O_3[61,62]. Even higher Mg solubilities could result from using an activated source, where the H chemical potential $\Delta\mu_H$ can exceed the thermodynamic limits. Such hydrogen plasma has been successfully used in the past during atomic layer deposition (ALD) growth of AlN[63] and for SiC surface cleaning prior to molecular beam epitaxy (MBE) growth of GaN[64]. In Figure 2b and the following discussion we consider non-equilibrium Mg concentrations up to 10%, since in

thin-film growth the thermodynamic solubility limit can often be exceeded due to slow exsolution kinetics[65]. For experimental reference, we note that in an ion implantation study[26] Mg dopant concentration up to 1.5×10^{19} cm^{-3} (about 0.05% of the 3.82×10^{22} cm^{-3} Ga sites) has been achieved in bulk substrates, and it is expected that still much higher concentrations are achievable in thin film growth.

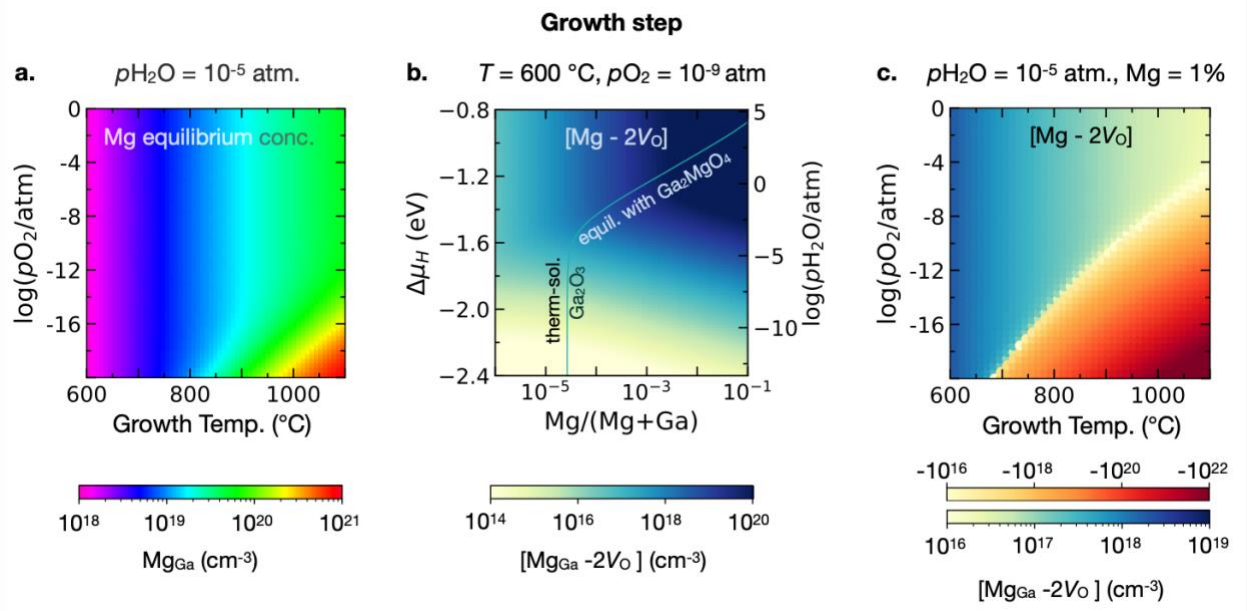

Figure 2. (a) Predicted Mg_{Ga} defect concentration as function of growth temperature (T_g) and O_2 partial pressure (pO_2). (b) Defect equilibria as a function of the Mg/(Mg+Ga) ratio and the water vapor partial pressure (pH_2O) under O-poor growth conditions typical for thin film growth. The solid line shows the Mg solubility limit and the color scale shows the dopant-defect difference concentration [$Mg_{Ga} – 2V_O$]. (c) [$Mg_{Ga} – 2V_O$] as function of T_g and pO_2 at 1% Mg doping.

Besides Mg solubility considerations, growth under hydrogen addition could also be utilized to minimize the contribution of intrinsic defects to the acceptor compensation[43]. If the compensation is dominated by H_i donors, the Mg acceptors could be activated by annealing out the hydrogen, proposed that the intrinsic defects would not re-equilibrate (see discussion below). To quantify this effect, we define the dopant-defect difference concentration [$Mg_{Ga} – 2V_O$] with the results shown as a color scale in Figure 2b. The significance of this number is that it equals the hypothetical net acceptor concentration if all hydrogen could be purged during the high temperature annealing step without introducing additional V_O defects. Therefore, we will refer to it as the “precursor” acceptor concentration. The color scale in Fig 2b shows [$Mg_{Ga} – 2V_O$] increasing moderately with Mg composition and rather strongly with pH_2O, and the associated H chemical potential. Thus, the hydrogen serves to reduce the intrinsic compensation mechanism, thereby maximizing the precursor acceptor concentration for the subsequent annealing step. Figure 2c explores the dependence of the [$Mg_{Ga} – 2V_O$] concentration as function of T and pO_2 at fixed pH_2O and Mg composition. We observe that this precursor acceptor density decreases with increasing growth temperature. Also, for too reducing conditions (too high T_g or too low pO_2),

[$Mg_{Ga} - 2V_O$] becomes negative, implying that the system would remain *n*-type even if all H were removed. Thus, low temperature conditions are favorable for the initial growth step.

IV. Annealing step

In the post-growth annealing step (Fig. 3), H-poor/O-rich conditions are considered, analogous to the H-poor/N-rich conditions used for Mg acceptor activation in GaN[40,41]. At 600°C, the O chemical potential increases from $\Delta\mu_O = -1.72$ to -0.94 eV as pO_2 increases from 10^{-9} atm in the growth step to 1 atm considered here for the O-rich annealing condition. Apart from increasing the formation energy of compensating O vacancies, the result is also a reduction of the H chemical potential from $\Delta\mu_H = -1.68$ (growth step with $pO_2 = 10^{-9}$ atm and $pH_2O = 10^{-5}$ atm) to -2.33 eV when taking $pH_2O = 10^{-8}$ atm (10 ppb) for purified O_2 at 1 atm used in the annealing step. Additionally, increasing the temperature during annealing lowers both $\Delta\mu_O$ and $\Delta\mu_H$, e.g., by about 0.4 eV between 600 and 900°C. Thus, the Mg acceptor activation relies on both suppressing compensation by V_O and reduction of the H concentration during annealing. Kinetically, the annealing conditions must also be such that H is sufficiently mobile to diffuse out while Mg remains immobile so to prevent Mg segregation. The rationale for choosing the present process parameters comes from recent Mg doping studies[26,28,66] , indicating that Mg needs $T >$ 800 °C to become mobile, and calculations of a small migration barrier of 0.34 eV[22] for H_i^+ indicating sufficiently fast H diffusion. A more subtle question is whether the annealing process can be performed such that the O vacancy concentrations from the growth step are maintained or whether they equilibrate. Since it could be feasible to realize either situation, we will consider both scenarios.

A. Annealing with V_O equilibration

In this scenario, only the total Mg concentration is carried over from the growth step, and all other degrees of freedom are equilibrated, while switching to the O-rich/H-poor regime ($pO_2 = 1$ atm, $pH_2O = 10^{-8}$ atm). Thus, in this scenario, the H addition of the growth step is relevant only in so far it supports the incorporation of Mg in the Ga_2O_3 lattice. Figure 3a shows the resulting net acceptor concentration [$Mg–2V_O–H_i$] obtained from thermodynamic modeling as function of annealing temperature. As the annealing temperature increases, H is purged out of the system, resulting in an increasing concentration of uncompensated net Mg acceptors, making the system net *p*-type in the sense of a positive value of the [$Mg - 2V_O - H_i$] concentration difference. However, as the annealing temperature is increased, the O vacancy concentration also increases (driven by a reduction of $\Delta\mu_O$) and therefore, there is a tipping point with respect to the annealing temperature above which O vacancies compensate the Mg acceptors and make the system net *n*-type.

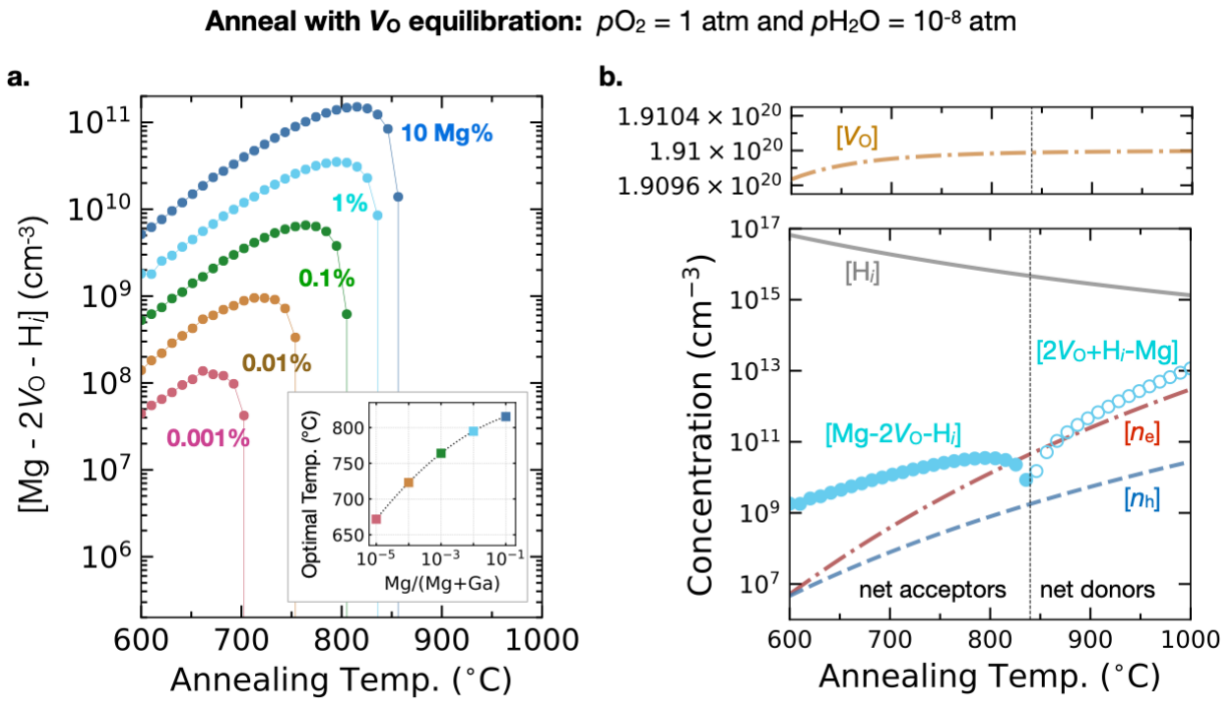

Figure 3. (a) Predicted net acceptor concentration [Mg – 2V_O – H$_i$] for the O-rich/H-poor annealing step. The inset shows the dependence of the optimal annealing temperature T_a on the Mg concentration. (b) The detailed defect equilibrium for Mg/(Mg+Ga) = 1%. The vertical dotted line indicates the crossover from net *p*-type to net *n*-type.

While the Fermi energy remains in the mid-gap region during annealing, it exhibits a small shift towards higher energies with increasing temperature, enough to affect the ratio between charged and ionized defects (Mg_{Ga}^0 vs Mg_{Ga}^- and V_O^0 vs V_O^{2+}). These changes in the order of 10^{10} cm^{-3} contribute to the charge balance and, ultimately, cause the crossover from net *p*-type to net *n*-type. As seen in the inset of Fig 3a, the optimum annealing temperature, i.e., the temperature at which the net *p*-type doping is maximized, increases from 670 to 820 °C with increasing Mg composition from 0.001% to 10%. The resulting net acceptor concentrations in the range of 10^8 - 10^{11} cm^{-3} are rather low, but the type conversion to net *p*-type is a significant hallmark, since it affords very low free electron densities at device operating conditions (see below). The resulting net acceptor density [Mg – 2V_O – H$_i$] is much lower than the precursor acceptor density [Mg – 2V_O] determined above for the growth step. This incomplete acceptor activation is due to the fact that not all hydrogen is purged, but also due to an increase of the concentration of compensating O vacancies during the annealing step, resulting from a lowered formation energy of V_O^{2+} as E_F is reduced, even as $\Delta\mu_O$ is increased compared to the growth step. Hence, a higher net *p*-type doping is expected for the case when V_O equilibration is suppressed, as discussed below.

The residual H concentration ranges from 1.5×10^{15} to 1.5×10^{16} cm^{-3} at the optimal temperature for the Mg doping level between 0.001% and 10%, respectively. There are two driving forces limiting the removal of hydrogen during the anneal. First, the reduction of the Fermi level lowers the formation energy of the positively charged H_i^+ interstitial. Second, with increasing

Mg doping level, the law of mass action increasingly impedes the dissociation the (Mg_{Ga}-H_i) defect pair. Specifically, the fraction of unpaired H_i^+ at the optimal annealing temperature (*cf*. Fig. 3a) decreases from 70% to 4% as the Mg doping level increases from 0.001% to 10%, even though the temperature increases concomitantly from 670 to 815 °C.

B. Annealing without V_O equilibration

We are also considering possible non-equilibrium annealing conditions in Ga_2O_3, even though these might be more difficult to realize experimentally. Under the assumption that O diffusion is much slower than that of H, the annealing process could be performed such that H diffuses out while the O vacancy formation does not have enough time to re-equilibrate. In this scenario, the V_O concentration is fixed to that of the preceding growth step, and the H addition during growth has higher significance than in the equilibrium annealing case, since it serves to reduce the compensation by V_O and thereby increase the precursor acceptor density [Mg – $2V_O$] (*cf*. Fig. 2b). The calculated values of O vacancy migration barriers in the literature[67] indeed indicate a much lower mobility compared to interstitial hydrogen[22]. Therefore, non-equilibrium annealing could be feasible if the annealing process is performed sufficiently fast. Even though the total V_O concentration remains constant, the dopant-defect pair association-dissociation process is equilibrated in the simulation, because this process does not require long-range diffusion and should be comparatively fast.

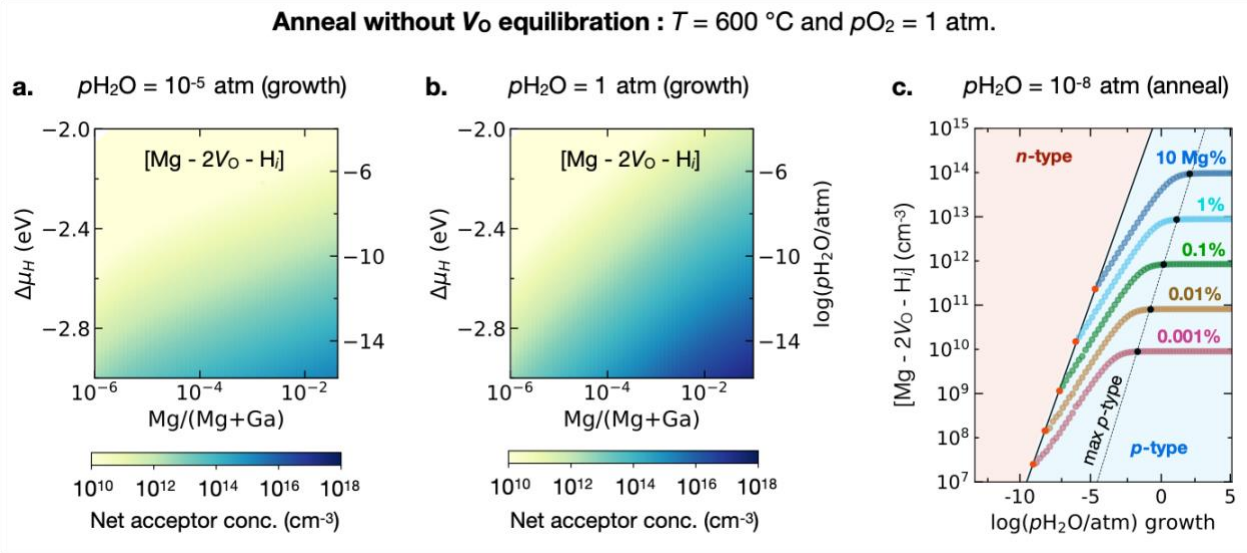

Figure 4. Predicted net acceptor concentration [Mg – $2V_O$ – H_i] under O-rich/H-poor annealing conditions at T_a = 600 °C and pO_2 = 1 atm, as function of Mg-doping level and pH_2O (controlling $\Delta\mu_H$) during the anneal. Non-equilibrium conditions are assumed such that the O-vacancy concentration of the preceding growth step is maintained. The underlying growth step conditions are consistent with Fig. 2b, i.e., T_g = 600 °C, pO_2 = 10^{-9} atm, with pH_2O = 10^{-5} atm in (a) and pH_2O = 1 atm in (b). The dependence of the net acceptor concentration on pH_2O during the growth step is shown in (c).

Figure 4 shows the predicted net acceptor concentration [Mg – $2V_O$ – H_i] for annealing without V_O equilibration. The underlying growth step conditions are identical to those considered above (*cf*. Fig. 2b), i.e., T_g = 600 °C, pO_2 = 10^{-9} atm, with hydrogen exposure during growth taken as

pH$_2$O = 10^{-5} atm for Fig. 4a and 1 atm for Fig 4b. For the annealing conditions, we maintain the same temperature, T_a = 600 °C and use O-rich conditions with pO$_2$ = 1 atm as in the equilibrium annealing case above. According to migration barrier calculations,[67] O vacancies are beginning to become mobile at this temperature. Note that the model here assumes equilibration of O vacancies during growth but not during annealing, despite the fact that both processes occur at same temperature. This assumption can be justified by the general observations that the surface kinetics during growth is usually faster than in the bulk, and the diffusion distance required for equilibration is much larger for the completed film during annealing than it is during deposition[68,69].

We observe in Fig. 4 the expected increase of the net acceptor density with increasing Mg-doping level and decreasing H-chemical potential $\Delta\mu_H$, which is determined by the corresponding pH$_2$O during the annealing. Compared to the annealing with V_O equilibration, the net acceptor density increases considerably under otherwise identical conditions. For example, for growth with 1% Mg doping and pH$_2$O = 10^{-5} atm, we obtain [Mg – 2V_O – H$_i$] ≈ 10^{11} cm^{-3} (Fig 4a) after non-equilibrium annealing at 600 °C and pH$_2$O = 10^{-8} atm (purified O$_2$), about 1-2 orders of magnitude higher than in case of annealing with V_O equilibration (*cf*. Fig. 3a). Higher net acceptor densities, up to 10^{14} cm^{-3} (Fig 4b), result when the preceding growth step is performed under very H rich conditions with pH$_2$O = 1 atm. These results suggest that H addition during growth is most impactful when choosing deposition techniques that allow for high H$_2$O partial pressures. As seen in Fig 4c, a minimum pH$_2$O must be supplied during growth to enable *p*-type conversion during non-equilibrium annealing, for example pH$_2$O = 10^{-7} atm for 1% Mg doping. In the absence of H$_2$O addition, the compensation is dominated by O vacancies during growth, preventing type conversion during annealing. The H$_2$O partial pressure required to achieve maximal net *p*-type doping increases from 10^{-2} atm to 10^{2} atm with increasing Mg concentration from 0.001% to 10%. These results provide theoretical guidance for optimization of the post-growth annealing step of Mg-doped Ga$_2$O$_3$.

V. Quench step to device operation conditions

Finally, we are considering the doping situation under device operating conditions. To this end, we simulate a "quench step", i.e., the cool-down after annealing, performed fast enough so that the defect concentrations do not re-equilibrate. It is assumed that the defect concentrations from the preceding annealing step are frozen-in as the temperature is quenched from the annealing temperature T_a to the operating temperature T_o, and no equilibration with the environment takes place (e.g., H uptake from ambient precluded by encapsulation). During this step, only the electronic degrees of freedom equilibrate, i.e., the Fermi level E_F re-adjusts such to satisfy the charge balance condition for the electron (n_e), hole (n_h), and charged defect concentrations at the lower T_o. We also assume that the defect pair and complex association-dissociation equilibrium is frozen-in during the quench, although this mechanism is not expected to significantly affect the Fermi level and carrier concentrations at T_o. We are considering elevated device operating temperatures T_o, as relevant for Ga$_2$O$_3$ high-power and high-temperature electronics applications[70]. Figure 5a shows the Fermi level as function of T_o and the Mg doping level for the case of V_O equilibration during the preceding annealing step at the optimum temperature T_a for any given Mg doping level (*cf*. Fig. 3 insert). Figures 5b and 5c are for the case of non-equilibrium annealing at 600 °C, where the growth step was performed at the same temperature with pH$_2$O = 10^{-5} atm and 1 atm, respectively (*cf*. Fig. 4a and 4b). In all cases, the

annealing conditions before the quench were taken at pO_2 = 1 atm and pH_2O = 10^{-8} atm as discussed above.

In Fig. 5a, we observe a moderate reduction of E_F with the Mg doping level. The Fermi level increases with operating temperature T_o, but remains within the lower half of the band gap (net *p*-type). While the absolute hole carrier concentration remains very low (below 10^6 cm^{-3}), the more important finding is here that the electron concentration remains negligible (below 10^3 cm^{-3}) up to 400 °C. Thus, electrons become minority carriers. The suppression of the electron density is an important feature of the type conversion, and our simulations suggest that the proposed growth-annealing process is suitable to effectively suppress the electron conductivity, e.g., for the purpose to minimize the associated leakage currents in device applications. However, achieving actual *p*-type conductivity is a much greater challenge. The quenching from the non-equilibrium annealing step, shown in Figs. 5b and 5c, affords a stronger Fermi level reduction than the annealing with V_O equilibration. Even then, however, the corresponding hole concentrations are only about 10^8 cm^{-3} at T_o = 400 °C (Fig. 5c). Since holes tend to form localized polarons rather than acting as band-like free carriers, the *p*-type conductivity is further limited by the hole mobility. Based on a predicted polaron hopping barrier of 0.4 eV, the mobility was estimated in Ref.[71] as 10^{-6} cm^2 V^{-1} s^{-1} at room temperature, which could increase to about 10^{-3} cm^2 V^{-1} s^{-1} at 400 °C, resulting in a conductivity $\sigma \approx 10^{-14}$ S/cm for the above mentioned hole density. These rough estimates illustrate the challenges for achieving significant *p*-type conductivity even at elevated temperatures and under optimistic assumptions about suppressing the V_O compensation mechanism.

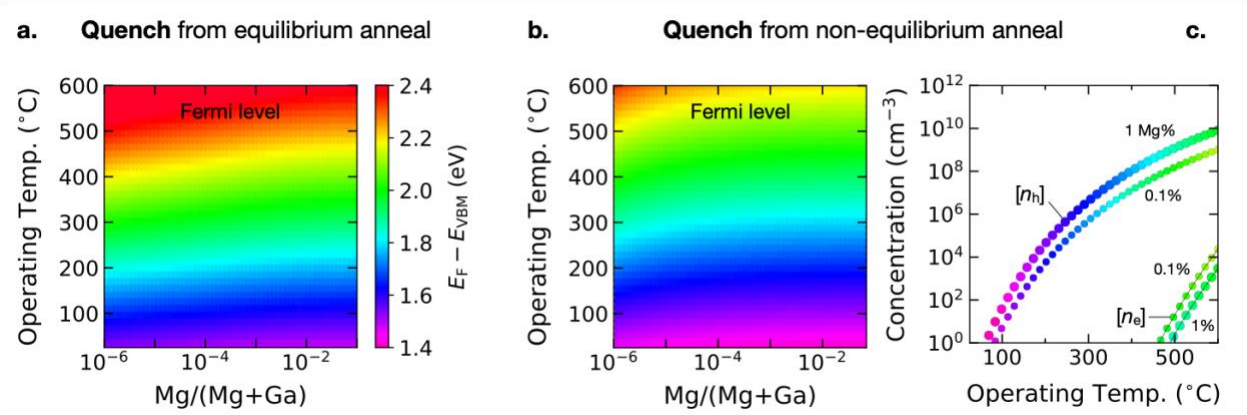

Figure 5. (a) Predicted Fermi level ($E_F - E_{VBM}$) as function of operating temperature T_o and Mg doping level, after quenching from the optimal T_a (inset in Fig. 3a) of the annealing step with V_O equilibration. (b) Fermi level after quench from the preceding annealing step at T_a = 600 °C without V_O equilibration with growth at pH_2O = 10^{-5} atm (*cf*. Fig. 4a), and (c) with growth at pH_2O = 1 atm (*cf*. Fig. 4b). The color scale for E_F shown in (a) applies throughout. In (c), the electron [n_e] and hole [n_h] concentrations corresponding to E_F at the respective T_o are shown explicitly for Mg concentrations of 0.1% and 1%.

The low free hole density and low polaronic hole mobility predicted in Ga_2O_3 indicate that it may be better to use other *p*-type oxide materials as Schottky or heterojunction partners to Ga_2O_3 for contact applications that require high electrical conductivity. Indeed, several recent

publications demonstrated promising diode performance with semiconductor NiO[72,73], Cu_2O[74,75], $PdCoO_2$[76,77], $ZnCo_2O_4$[78] heterojunction contacts and various oxidized precious metal contacts (e.g. metallic IrO_x, PtO_x, PdO_x, RuO_x Schottky contacts)[79,80] to Ga_2O_3. However, the ability of these Schottky and heterojunction partners to achieve large built-in electric field at the interface with Ga_2O_3 may be limited, because it requires large work function of the *p*-type contact material, and because the resulting Ga2O3 device performance would be limited by breakdown in this lower-bandgap p-type contact. The typical work functions of the aforementioned materials are in the 4-6 eV range[81–84], which is just 0-2 eV higher compared to the 4 eV work function of n-type Ga_2O_3[85–87], providing limited built-in field at the heterointerface. In contrast, our predictions (Fig. 5) show that the work function of the Fermi level engineered Ga_2O_3 can be 1.4 eV above the valence band, which corresponds to a work function in the 7 - 8 eV range. This higher work function can provide larger built-it field at interfaces between *n*-type Ga_2O_3 and device layers that do not require high electrical conductivity. Example of such applications include blocking layers around current apertures of unipolar enhancement-mode (normally-off) MOSFETs or edge termination structures in vertical Schottky Barrier Diodes (SBDs). Another advantage for these applications would be the possibility of high-quality homoepitaxial regrowth (selective area epitaxy[55,88]) of *n*-type Ga_2O_3 on top of this Fermi level engineered Ga_2O_3, which would not be possible if foreign oxide or metal materials are used in such devices.

VI. Computational details

The first-principles calculations were performed using the projector augmented wave (PAW) method[89] as implemented in the VASP (Vienna Ab-initio Simulation Package) code[90] for DFT[91], hybrid-DFT[92], and *GW*[93] calculations. The generalized gradient approximation (GGA) of Ref[94] was used for DFT exchange and correlation and the HSE06[95,96] functional for hybrid functional calculations. For the dopants, defects, and their pairs and complexes, we used a 160 atom supercell with a Γ-centered 2×2×2 k-mesh, and performed the calculations using our recently developed automated defect framework[97]. Finite supercell size corrections are applied as described in Ref.[98] All compound formation enthalpies and defect formation energies were calculated at the GGA level, except for the charge neutral Mg_{Ga} acceptors, which are polaronic open-shell states whose localized nature is not captured by standard DFT. To include the neutral Mg acceptor in the defect equilibrium, we calculated the (0/1−) charge transition levels for Mg_{Ga1} and Mg_{Ga2} with the hybrid functional, using α = 0.30 and μ_{rs} = 0.2 $Å^{-1}$ for the Fock exchange and the range separation parameters, respectively. For the band gap corrections of the defect formation energies according to Ref[48], we performed *GW* calculations[99] to obtain the band edge shifts of ΔE_{VBM} = −1.82 eV and ΔE_{CBM} = +1.10 eV relative to DFT-GGA, resulting in the bandgap value of 4.96 eV.

The PAW potentials “Ga_d”, “O”, “O_s”, “Mg_pv”, and “H” of the VASP 4.6 distribution were used. For structures without hydrogen, the soft “O_s” potential was employed with a plane wave energy cutoff of 340 eV. Previous tests have confirmed that such calculations are accurate for sufficiently large interatomic distances.[48] Due to the presence of short O-H bonds for which the soft potential may not be accurate, we used the standard “O” potential with 520 eV cutoff for structures with hydrogen. The FERE reference elemental chemical potentials of Ref[49] are used for Ga, O, and Mg. For hydrogen, we determined here the value μ_H^{FERE} = −3.49 eV by fitting against the tabulated formation enthalpies[54] of the following compounds, H_2O (ice I_h), LiH, MgH_2,

LiOH and $Mg(OH)_2$. The temperature dependence of the CBM was taken from Ref[23], where it was determined from molecular dynamics simulations.

Table 2: Calculated defect formation energies ΔH_{ref} at the reference point ($\Delta E_F = \Delta\mu_i = 0$).

Defect	ΔH_{ref} (eV)	Defect	ΔH_{ref} (eV)
V_{O1}^{2+}	–2.53	$(Mg_{Ga2}^{1-} + V_{O1}^{2+})^{1+}$	–1.15
V_{O1}^{0}	+4.53	$(Mg_{Ga2}^{1-} + V_{O1}^{0})^{1-}$	+6.45
V_{O2}^{2+}	–1.83	$(Mg_{Ga2}^{1-} + V_{O2}^{2+})^{1+}$	–0.29
V_{O2}^{0}	+4.08	$(Mg_{Ga2}^{1-} + V_{O2}^{0})^{1-}$	+5.98
V_{O3}^{2+}	–2.66	$(Mg_{Ga2}^{1-} + V_{O3}^{2+})^{1+}$	–1.16
V_{O3}^{0}	+4.72	$(Mg_{Ga2}^{1-} + V_{O3}^{0})^{1-}$	+6.79
V_{Ga1}^{3-}	+16.71	$(Mg_{Ga2}^{1-} + H_i^{1+})^{0}$	–1.87
V_{Ga2}^{3-}	+17.33	$(2Mg_{Ga2}^{1-} + V_{O1}^{2+})^{0}$	+0.68
Mg_i^{2+}	–6.69	$(2Mg_{Ga2}^{1-} + V_{O1}^{0})^{2-}$	+8.90
Mg_{Ga1}^{1-}	+2.59	$(2Mg_{Ga2}^{1-} + V_{O3}^{2+})^{0}$	+0.53
Mg_{Ga2}^{1-}	+2.12	$(2Mg_{Ga2}^{1-} + V_{O3}^{0})^{2-}$	+8.98
H_i^{1+}	–3.60		

VII. Conclusions

We performed a thermodynamic simulation of a three-step synthesis process (growth-annealing-quench sequence) for hydrogen-assisted magnesium acceptor doping in Ga_2O_3 based on defect energies obtained from first principles calculations. During the first growth step, the thermodynamic solubility limit of Mg acceptor dopants is significantly increased for partial pressures above $pH_2O > 10^{-5}$ atm. The H exposure during growth also serves to reduce the acceptor compensation through V_O defects. The second annealing step at O-rich/H-poor conditions ($pO_2 = 1$ atm and $pH_2O = 10^{-8}$ atm) can produce a doping type conversion from net *n*- to net *p*-type, regardless of the assumptions made about V_O re-equilibration. For the case with V_O equilibration, there is an optimal annealing temperature at which the net *p*-type doing is maximized, e.g., about 800 °C for 1% Mg doping, but too high annealing temperatures result in doping reversion back to net *n*-type. The net *p*-type doping can be further increased if the V_O equilibration can be suppressed, e.g., in rapid thermal processing at lower temperature (600 °C). In this case, the H added during growth not only supports the Mg solubility, but is also essential to suppress the intrinsic O vacancy compensation mechanism. Even though neither of these two scenarios creates significant *p*-type conductivity, we predict doping type conversion and an associated drop of the Fermi level down to 1.5 eV above the valence band after the third quenching step. This Fermi level engineered Ga_2O_3 presents important opportunities for electronic device design, allowing to create a significant built-in field with an adjoining *n*-type material, and greatly suppressing the free electron density. The specific predictions of suitable synthesis process conditions presented in this paper could guide the fabrication of current blocking layers in normally-off (enhancement-mode) vertical Ga_2O_3 based MOSFET, and edge termination structures in vertical Schottky barrier diodes with increased breakdown voltage. In the future, similar computational approach can be used to predict suitable synthesis conditions and doping protocols for other emerging ultra wide band gap semiconductors.

Acknowledgements

This work was funded by the U.S. Department of Energy (DOE), through the Laboratory Directed Research and Development Program of the National Renewable Energy Laboratory (NREL), and by the DOE Advanced Manufacturing Office of the Office of Energy Efficiency and Renewable Energy (EERE). The Alliance for Sustainable Energy, LLC, operates and manages NREL under contract DE-AC36-08GO28308. This work used High-Performance Computing resources at NREL, sponsored by DOE-EERE. The views expressed in the article do not necessarily represent the views of the DOE or the U.S. government.

Data Availability

The data that support the findings of this study are available from the corresponding author upon reasonable request.

References:

1. Pearton, S. J. *et al.* A review of Ga2O3 materials, processing, and devices. *Appl. Phys. Rev.* **5**, 011301 (2018).
2. Reese, S. B., Remo, T., Green, J. & Zakutayev, A. How Much Will Gallium Oxide Power Electronics Cost? *Joule* **3**, 903–907 (2019).
3. Baldini, M., Galazka, Z. & Wagner, G. Recent progress in the growth of β-Ga2O3 for power electronics applications. *Mater. Sci. Semicond. Process.* **78**, 132–146 (2018).
4. Liu, Z. *et al.* Review of gallium oxide based field-effect transistors and Schottky barrier diodes. *Chinese Phys. B* **28**, 017105 (2019).
5. Chabak, K. D. *et al.* Lateral β -Ga 2 O 3 field effect transistors. *Semicond. Sci. Technol.* **35**, 013002 (2020).
6. Xu, J., Zheng, W. & Huang, F. Gallium oxide solar-blind ultraviolet photodetectors: a review. *J. Mater. Chem. C* **7**, 8753–8770 (2019).
7. Chen, X., Ren, F., Gu, S. & Ye, J. Review of gallium-oxide-based solar-blind ultraviolet photodetectors. *Photonics Res.* **7**, 381 (2019).
8. Chen, X., Ren, F., Ye, J. & Gu, S. Gallium oxide-based solar-blind ultraviolet photodetectors. *Semicond. Sci. Technol.* **35**, 023001 (2020).
9. Hoefer, U., Frank, J. & Fleischer, M. High temperature Ga2O3-gas sensors and SnO2-gas sensors: a comparison. *Sensors Actuators B Chem.* **78**, 6–11 (2001).
10. Afzal, A. β-Ga2O3 nanowires and thin films for metal oxide semiconductor gas sensors: Sensing mechanisms and performance enhancement strategies. *J. Mater.* **5**, 542–557 (2019).
11. Minami, T., Nishi, Y. & Miyata, T. High-Efficiency Cu2O-Based Heterojunction Solar Cells Fabricated Using a Ga2O3 Thin Film as N-Type Layer. *Appl. Phys. Express* **6**, 044101 (2013).
12. Chua, D., Kim, S. B. & Gordon, R. Enhancement of the open circuit voltage of Cu2O/Ga2O3 heterojunction solar cells through the mitigation of interfacial recombination. *AIP Adv.* **9**, 055203 (2019).
13. Li, Y. *et al.* Efficient Assembly of Bridged β-Ga2O3 Nanowires for Solar-Blind Photodetection. *Adv. Funct. Mater.* **20**, 3972–3978 (2010).
14. Yang, J.-B. *et al.* Resistive switching characteristics of gallium oxide for nonvolatile memory application. *Thin Solid Films* **529**, 200–204 (2013).

15. Higashiwaki, M. *et al.* Recent progress in Ga2O3 power devices. *Semicond. Sci. Technol.* **31**, 034001 (2016).
16. Pearton, S. J., Ren, F., Tadjer, M. & Kim, J. Perspective: Ga2O3 for ultra-high power rectifiers and MOSFETS. *J. Appl. Phys.* **124**, 220901 (2018).
17. Wong, M. H., Goto, K., Murakami, H., Kumagai, Y. & Higashiwaki, M. Current Aperture Vertical β-Ga2O3 MOSFETs Fabricated by N- and Si-Ion Implantation Doping. *IEEE Electron Device Lett.* **40**, 431–434 (2019).
18. Hu, Z. *et al.* Enhancement-Mode Ga2O3 Vertical Transistors With Breakdown Voltage >1 kV. *IEEE Electron Device Lett.* **39**, 869–872 (2018).
19. Ueda, N., Hosono, H., Waseda, R. & Kawazoe, H. Synthesis and control of conductivity of ultraviolet transmitting β-Ga2O3 single crystals. *Appl. Phys. Lett.* **70**, 3561–3563 (1997).
20. Sasaki, K. *et al.* Device-Quality β-Ga2O3 Epitaxial Films Fabricated by Ozone Molecular Beam Epitaxy. *Appl. Phys. Express* **5**, 035502 (2012).
21. Ahmadi, E. *et al.* Ge doping of β-Ga 2 O 3 films grown by plasma-assisted molecular beam epitaxy. *Appl. Phys. Express* **10**, 041102 (2017).
22. Varley, J. B., Weber, J. R., Janotti, A. & Van de Walle, C. G. Oxygen vacancies and donor impurities in β-Ga2O3. *Appl. Phys. Lett.* **97**, 142106 (2010).
23. Lany, S. Defect phase diagram for doping of Ga2O3. *APL Mater.* **6**, 046103 (2018).
24. Varley, J. B., Peelaers, H., Janotti, A. & Van de Walle, C. G. Hydrogenated cation vacancies in semiconducting oxides. *J. Phys. Condens. Matter* **23**, 334212 (2011).
25. Kyrtsos, A., Matsubara, M. & Bellotti, E. On the feasibility of p-type Ga2O3. *Appl. Phys. Lett.* **112**, 032108 (2018).
26. Wong, M. H. *et al.* Acceptor doping of β-Ga2O3 by Mg and N ion implantations. *Appl. Phys. Lett.* **113**, 102103 (2018).
27. Lyons, J. L. A survey of acceptor dopants for β-Ga2O3. *Semicond. Sci. Technol.* **33**, 05LT02 (2018).
28. Peelaers, H., Lyons, J. L., Varley, J. B. & Van de Walle, C. G. Deep acceptors and their diffusion in Ga 2 O 3. *APL Mater.* **7**, 022519 (2019).
29. Chikoidze, E. *et al.* Enhancing the intrinsic p-type conductivity of the ultra-wide bandgap Ga 2 O 3 semiconductor. *J. Mater. Chem. C* **7**, 10231–10239 (2019).
30. Zhang, J., Shi, J., Qi, D.-C., Chen, L. & Zhang, K. H. L. Recent progress on the electronic structure, defect, and doping properties of Ga2O 3. *APL Mater.* **8**, 020906 (2020).
31. McCluskey, M. D. Point defects in Ga 2 O 3. *J. Appl. Phys.* **127**, 101101 (2020).
32. Feng, Z., Bhuiyan, A. F. M. A. U., Kalarickal, N. K., Rajan, S. & Zhao, H. Mg acceptor doping in MOCVD (010) β-Ga2O3. *Appl. Phys. Lett.* **117**, 222106 (2020).
33. Lenyk, C. A., Gustafson, T. D., Basun, S. A., Halliburton, L. E. & Giles, N. C. Experimental determination of the (0/−) level for Mg acceptors in β -Ga 2 O 3 crystals. *Appl. Phys. Lett.* **116**, 142101 (2020).
34. Su, Y. *et al.* Deep level acceptors of Zn-Mg divalent ions dopants in β-Ga2O3 for the difficulty to p-type conductivity. *J. Alloys Compd.* **782**, 299–303 (2019).
35. Ho, Q. D., Frauenheim, T. & Deák, P. Theoretical confirmation of the polaron model for the Mg acceptor in β-Ga 2 O 3. *J. Appl. Phys.* **124**, 145702 (2018).
36. Gake, T., Kumagai, Y. & Oba, F. First-principles study of self-trapped holes and acceptor impurities in Ga2O3 polymorphs. *Phys. Rev. Mater.* **3**, 44603 (2019).
37. Skachkov, D. & Lambrecht, W. R. L. Computational study of electron paramagnetic resonance parameters for Mg and Zn impurities in β -Ga 2 O 3. *Appl. Phys. Lett.* **114**, 202102 (2019).
38. Frodason, Y. K., Johansen, K. M., Vines, L. & Varley, J. B. Self-trapped hole and impurity-related broad luminescence in β-Ga2O3. *J. Appl. Phys.* **127**, 075701 (2020).
39. Kotecha, R., Metzger, W., Mather, B., Narumanchi, S. & Zakutayev, A. Modeling and

Analysis of Gallium Oxide Vertical Transistors. *ECS J. Solid State Sci. Technol.* **8**, Q3202–Q3205 (2019).
40. Nakamura, S., Iwasa, N., Senoh, M. & Mukai, T. Hole Compensation Mechanism of P-Type GaN Films. *Jpn. J. Appl. Phys.* **31**, 1258–1266 (1992).
41. Nakamura, S., Mukai, T., Senoh, M. & Iwasa, N. Thermal Annealing Effects on P-Type Mg-Doped GaN Films. *Jpn. J. Appl. Phys.* **31**, L139–L142 (1992).
42. Vechten, J. A. Van, Zook, J. D., Horning, R. D. & Goldenberg, B. Defeating Compensation in Wide Gap Semiconductors by Growing in H that is Removed by Low Temperature De-Ionizing Radiation. *Jpn. J. Appl. Phys.* **31**, 3662–3663 (1992).
43. Neugebauer, J. & Van De Walle, C. G. Role of hydrogen in doping of GaN. *Appl. Phys. Lett.* **68**, 1829–1831 (1996).
44. Neumark, G. F. Wide bandgap light-emitting devices materials and doping problems. *Mater. Lett.* **30**, 131–135 (1997).
45. Fioretti, A. N. *et al.* Effects of Hydrogen on Acceptor Activation in Ternary Nitride Semiconductors. *Adv. Electron. Mater.* **3**, 1600544 (2017).
46. Pan, J. *et al.* Interplay between Composition, Electronic Structure, Disorder, and Doping due to Dual Sublattice Mixing in Nonequilibrium Synthesis of ZnSnN 2 :O. *Adv. Mater.* **31**, 1807406 (2019).
47. Kim, J. *et al.* Influence of hydrogen and oxygen on the structure and properties of sputtered magnesium zirconium oxynitride thin films. *J. Mater. Chem. A* **8**, 9364–9372 (2020).
48. Peng, H. *et al.* Convergence of density and hybrid functional defect calculations for compound semiconductors. *Phys. Rev. B* **88**, 115201 (2013).
49. Stevanović, V., Lany, S., Zhang, X. & Zunger, A. Correcting density functional theory for accurate predictions of compound enthalpies of formation: Fitted elemental-phase reference energies. *Phys. Rev. B* **85**, 115104 (2012).
50. Lany, S. Predicting polaronic defect states by means of generalized Koopmans density functional calculations. *Phys. status solidi* **248**, 1052–1060 (2011).
51. Kananen, B. E. *et al.* Electron paramagnetic resonance study of neutral Mg acceptors in β-Ga 2 O 3 crystals. *Appl. Phys. Lett.* **111**, 072102 (2017).
52. Biswas, K. & Lany, S. Energetics of quaternary III-V alloys described by incorporation and clustering of impurities. *Phys. Rev. B* **80**, 115206 (2009).
53. Lany, S. Communication: The electronic entropy of charged defect formation and its impact on thermochemical redox cycles. *J. Chem. Phys.* **148**, 071101 (2018).
54. Wagman, D. D. *et al.* 'The NBS tables of chemical thermodynamic properties: Selected values for inorganic and c1 and c2 organic substances in SI Units'. *J. Phys. Chem. Ref. Data* **11**, Suppl. 2 (1982).
55. Debald, A., Kotzea, S., Heuken, M., Kalisch, H. & Vescan, A. Growth and Characterization of Vertical and Lateral p-n Junctions Formed by Selective-Area p-GaN MOVPE on Patterned Templates. *Phys. status solidi* **216**, 1800677 (2019).
56. Zakutayev, A., Perry, N. H., Mason, T. O., Ginley, D. S. & Lany, S. Non-equilibrium origin of high electrical conductivity in gallium zinc oxide thin films. *Appl. Phys. Lett.* **103**, 232106 (2013).
57. Zunger, A. Practical doping principles. *Appl. Phys. Lett.* **83**, 57–59 (2003).
58. Van de Walle, C. G. & Neugebauer, J. Universal alignment of hydrogen levels in semiconductors, insulators and solutions. *Nature* **423**, 626–628 (2003).
59. Ingram, B. J., Gonzalez, G. B., Kammler, D. R., Bertoni, M. I. & Mason, T. O. Chemical and structural factors governing transparent conductivity in oxides. *J. Electroceramics* **13**, 167–175 (2004).
60. Brooks Tellekamp, M., Heinselman, K. N., Harvey, S., Khan, I. S. & Zakutayev, A. Growth and characterization of homoepitaxial β-Ga2O3 layers. *J. Phys. D. Appl. Phys.* **53**,

484002 (2020).
61. Terasako, T., Ichinotani, H. & Yagi, M. Growth of β-gallium oxide films and nanostructures by atmospheric- pressure CVD using gallium and water as source materials. *Phys. Status Solidi C.* **12**, 985–988 (2015).
62. Terasako, T., Kawasaki, Y. & Yagi, M. Growth and morphology control of β-Ga2O3 nanostructures by atmospheric-pressure CVD. *Thin Solid Films* **620**, 23–29 (2016).
63. Tian, L. *et al.* Aluminum nitride thin films deposited by hydrogen plasma enhanced and thermal atomic layer deposition. *Surf. Coatings Technol.* **347**, 181–190 (2018).
64. Lin, M. E. *et al.* GaN grown on hydrogen plasma cleaned 6H-SiC substrates. *Appl. Phys. Lett.* **62**, 702–704 (1993).
65. González, G. B., Mason, T. O., Okasinski, J. S., Buslaps, T. & Honkimäki, V. Determination of the Solubility of Tin in Indium Oxide Using In Situ and Ex Situ X-Ray Diffraction. *J. Am. Ceram. Soc.* **95**, 809–815 (2012).
66. Wong, M. H. *et al.* All-ion-implanted planar-gate current aperture vertical Ga 2 O 3 MOSFETs with Mg-doped blocking layer. *Appl. Phys. Express* **11**, 064102 (2018).
67. Kyrtsos, A., Matsubara, M. & Bellotti, E. Migration mechanisms and diffusion barriers of vacancies in Ga2O3. *Phys. Rev. B* **95**, 245202 (2017).
68. Mazzolini, P. & Bierwagen, O. Towards smooth (010) β-Ga2O3 films homoepitaxially grown by plasma assisted molecular beam epitaxy: the impact of substrate offcut and metal-to-oxygen flux ratio. *J. Phys. D. Appl. Phys.* **53**, 354003 (2020).
69. Bin Anooz, S. *et al.* Step flow growth of β -Ga2O3thin films on vicinal (100) β -Ga2O3substrates grown by MOVPE. *Appl. Phys. Lett.* **116**, 2–7 (2020).
70. Paret, P. *et al.* Thermal and Thermomechanical Modeling to Design a Gallium Oxide Power Electronics Package. in *2018 IEEE 6th Workshop on Wide Bandgap Power Devices and Applications (WiPDA)* 287–294 (IEEE, 2018).
71. Varley, J. B., Janotti, A., Franchini, C. & Van de Walle, C. G. Role of self-trapping in luminescence and p-type conductivity of wide-band-gap oxides. *Phys. Rev. B* **85**, 081109 (2012).
72. Kokubun, Y., Kubo, S. & Nakagomi, S. All-oxide p–n heterojunction diodes comprising p-type NiO and n-type β-Ga 2 O 3. *Appl. Phys. Express* **9**, 091101 (2016).
73. Wang, C. *et al.* Demonstration of the p-NiO x /n-Ga2O3 Heterojunction Gate FETs and Diodes With BV 2 /R on,sp Figures of Merit of 0.39 GW/cm 2 and 1.38 GW/cm 2. *IEEE Electron Device Lett.* **42**, 485–488 (2021).
74. Watahiki, T. *et al.* Heterojunction p-Cu 2 O/n-Ga2O3 diode with high breakdown voltage. *Appl. Phys. Lett.* **111**, 222104 (2017).
75. Tadjer, M. J., Luna, L. E., Cleveland, E., Hobart, K. D. & Kub, F. J. (Invited) Fabrication and Characterization of β-Ga 2 O 3 Heterojunction Rectifiers. *ECS Trans.* **85**, 21–26 (2018).
76. Harada, T., Ito, S. & Tsukazaki, A. Electric dipole effect in PdCoO 2 /β-Ga2O3 Schottky diodes for high-temperature operation. *Sci. Adv.* **5**, eaax5733 (2019).
77. Sun, J. *et al.* Growth of PdCoO 2 by ozone-assisted molecular-beam epitaxy. *APL Mater.* **7**, 121112 (2019).
78. Schlupp, P., Splith, D., von Wenckstern, H. & Grundmann, M. Electrical Properties of Vertical p-NiO/n-Ga 2 O 3 and p-ZnCo 2 O 4 /n-Ga 2 O 3 pn-Heterodiodes. *Phys. status solidi* **216**, 1800729 (2019).
79. Hou, C., Gazoni, R. M., Reeves, R. J. & Allen, M. W. Oxidized Metal Schottky Contacts on (010) β-Ga_2O_3. *IEEE Electron Device Lett.* **40**, 337–340 (2019).
80. Hou, C. *et al.* High temperature (500 °C) operating limits of oxidized platinum group metal (PtOx , IrOx , PdOx , RuOx) Schottky contacts on β -Ga2O3. *Appl. Phys. Lett.* **117**, 203502 (2020).
81. Chalamala, B. R. *et al.* Effect of growth conditions on surface morphology and

photoelectric work function characteristics of iridium oxide thin films. *Appl. Phys. Lett.* **74**, 1394–1396 (1999).
82. Steirer, K. X. *et al.* Solution deposited NiO thin-films as hole transport layers in organic photovoltaics. *Org. Electron.* **11**, 1414–1418 (2010).
83. Siol, S. *et al.* Band Alignment Engineering at Cu2O/ZnO Heterointerfaces. *ACS Appl. Mater. Interfaces* **8**, 21824–21831 (2016).
84. Zakutayev, A. *et al.* Zn-Ni-Co-O wide-band-gap p-type conductive oxides with high work functions. *MRS Commun.* **1**, 23–26 (2011).
85. Tak, B. R. *et al.* Point defects induced work function modulation of β-Ga2O3. *Appl. Surf. Sci.* **465**, 973–978 (2019).
86. Mohamed, M. *et al.* Schottky barrier height of Au on the transparent semiconducting oxide β -Ga 2 O 3. *Appl. Phys. Lett.* **101**, 132106 (2012).
87. Liu, Z. *et al.* Energy-band alignments at ZnO/Ga 2 O 3 and Ta2O5/Ga2O3 heterointerfaces by X-ray photoelectron spectroscopy and electron affinity rule. *J. Appl. Phys.* **126**, 045707 (2019).
88. Chang, A. S. *et al.* Selective Area Regrowth Produces Nonuniform Mg Doping Profiles in Nonplanar GaN p–n Junctions. *ACS Appl. Electron. Mater.* **3**, 704–710 (2021).
89. Blöchl, P. E. Projector augmented-wave method. *Phys. Rev. B* **50**, 17953–17979 (1994).
90. Kresse, G. & Furthmüller, J. Efficiency of ab-initio total energy calculations for metals and semiconductors using a plane-wave basis set. *Comput. Mater. Sci.* **6**, 15–50 (1996).
91. Kresse, G. From ultrasoft pseudopotentials to the projector augmented-wave method. *Phys. Rev. B* **59**, 1758–1775 (1999).
92. Paier, J. *et al.* Screened hybrid density functionals applied to solids. *J. Chem. Phys.* **124**, 154709 (2006).
93. Shishkin, M. & Kresse, G. Implementation and performance of the frequency-dependent GW method within the PAW framework. *Phys. Rev. B* **74**, 035101 (2006).
94. Perdew, J. P., Burke, K. & Ernzerhof, M. Generalized Gradient Approximation Made Simple. *Phys. Rev. Lett.* **77**, 3865–3868 (1996).
95. Heyd, J., Scuseria, G. E. & Ernzerhof, M. Hybrid functionals based on a screened Coulomb potential. *J. Chem. Phys.* **118**, 8207–8215 (2003).
96. Heyd, J., Scuseria, G. E. & Ernzerhof, M. Erratum: “Hybrid functionals based on a screened Coulomb potential” [J. Chem. Phys. 118, 8207 (2003)]. *J. Chem. Phys.* **124**, 219906 (2006).
97. Goyal, A., Gorai, P., Peng, H., Lany, S. & Stevanović, V. A computational framework for automation of point defect calculations. *Comput. Mater. Sci.* **130**, 1–9 (2017).
98. Lany, S. & Zunger, A. Accurate prediction of defect properties in density functional supercell calculations. *Model. Simul. Mater. Sci. Eng.* **17**, 084002 (2009).
99. Hedin, L. New Method for Calculating the One-Particle Green’s Function with Application to the Electron-Gas Problem. *Phys. Rev.* **139**, A796–A823 (1965).